Geophysical Research Letters

RESEARCH LETTER
10.1029/2024GL108220

Underthrusting of Tarim Lower Crust Beneath the Tibetan Plateau Revealed by Receiver Function Imaging

Chenglong Wu[1,2], Tao Xu[1,2], Xiaobo Tian[2,3], Ross N. Mitchell[3,4], Jiyan Lin[5], Jianfeng Yang[3,4], Xin Wang[6], and Zhanwu Lu[7]

[1]Key Laboratory of Mineral Resources, Institute of Geology and Geophysics, Chinese Academy of Sciences, Beijing, China, [2]Innovation Academy for Earth Science, CAS, Beijing, China, [3]State Key Laboratory of Lithospheric Evolution, Institute of Geology and Geophysics, Chinese Academy of Sciences, Beijing, China, [4]College of Earth and Planetary Sciences, University of Chinese Academy of Sciences, Beijing, China, [5]Geophysical Exploration Center, China Earthquake Administration, Zhengzhou, China, [6]Key Laboratory of Earth and Planetary Physics, Institute of Geology and Geophysics, Chinese Academy of Sciences, Beijing, China, [7]Institute of Geology, Chinese Academy of Geological Sciences, Beijing, China

Abstract The left-lateral Altyn Tagh Fault (ATF) system is the northern boundary of the Tibetan Plateau resulted from the India–Eurasia continental collision. How intracontinental deformation across the central ATF responds to the distal collision remains elusive, primarily due to unclear crustal structure. We obtained detailed crustal structure across the central ATF using receiver functions recorded by ∼NW–SE oriented linear dense array. The images reveal the Tarim lower crust is underthrusting beneath the Tibetan Plateau and reaches to a maximum depth of ∼75 km and undergoing partial eclogitization. The two south-dipping interfaces imaged beneath the Altyn Tagh Range (ATR) represent the thrusting Northern Altyn Fault and its branch fault. Oblique convergent forces extruded upper crustal materials along the thrust faults, creating the pop-up structure of ATR, supported by low Vp/Vs ratios. Our balanced cross-section for the Moho suggests intracontinental deformation in the ATR has accelerated since the late Miocene.

Plain Language Summary The Altyn Tagh Fault (ATF), serving as the northern boundary of the Tibetan Plateau, demarcates the Tarim Basin from the Qaidam Basin. Understanding how intracontinental deformation across the boundary region would better inform the uplift and expansion of the plateau. This study reveals the fine crustal structure by analyzing seismic data from a ∼NW–SE oriented linear dense array across the central ATF. Combined with fault slip rates, we propose that the Tarim lower crust is underthrusting beneath the Tibetan Plateau, leading to the extrusion of upper crustal materials and the rapid uplift of the Altyn Tagh Range since the late Miocene, which provides insight into the lateral growth of the plateau.

Key Points:

- Detailed crustal structure beneath the central Altyn Tagh Fault was imaged by receiver functions of a dense 2-D seismic array
- The Tarim lower crust is underthrusting to ∼75 km depth beneath the Tibetan Plateau
- The Altyn Tagh range was uplifted rapidly since late Miocene through the thickening of the upper crust

Supporting Information:

Supporting Information may be found in the online version of this article.

Correspondence to:

T. Xu and R. N. Mitchell,
xutao@mail.iggcas.ac.cn;
ross.mitchell@mail.iggcas.ac.cn

Citation:

Wu, C., Xu, T., Tian, X., Mitchell, R. N., Lin, J., Yang, J., et al. (2024). Underthrusting of Tarim lower crust beneath the Tibetan Plateau revealed by receiver function imaging. *Geophysical Research Letters*, *51*, e2024GL108220. https://doi.org/10.1029/2024GL108220

Received 8 JAN 2024
Accepted 15 JAN 2024

Author Contributions:

Conceptualization: Chenglong Wu, Tao Xu, Ross N. Mitchell
Data curation: Chenglong Wu, Jiyan Lin
Formal analysis: Chenglong Wu, Tao Xu, Xiaobo Tian, Xin Wang
Funding acquisition: Tao Xu, Zhanwu Lu
Investigation: Chenglong Wu, Ross N. Mitchell
Methodology: Chenglong Wu, Xiaobo Tian
Resources: Jiyan Lin, Zhanwu Lu
Supervision: Tao Xu
Writing – original draft: Chenglong Wu, Tao Xu

1. Introduction

The Cenozoic India–Eurasia collision has resulted in the uplift of the Tibetan Plateau, as well as the activation of major boundary faults such as the Altyn Tagh Fault (ATF) (Yin & Harrison, 2000). The left-lateral ATF system is one of the most prominent active strike-slip fault systems on Earth (Molnar & Dayem, 2010), which marks the boundary between the Tarim Basin and the northern Tibetan Plateau. Far-field effects of the India–Eurasia continental collision have induced the continuous northward migration of the northern boundary of the Tibetan Plateau by incorporating the neighboring rigid blocks (Hu et al., 2022; Tapponnier et al., 2001; Tian et al., 2021). Hence, investigating the intracontinental deformation across the ATF system contributes to our understanding of the uplift and expansion of the plateau.

The ATF system primarily comprises the 1,600-km-long left-lateral ATF trending ENE, and the North Altyn Fault (NAF) to the north of the central ATF as well as the prism-shaped Altyn Tagh Range (ATR) between them (Figure 1, Cowgill et al., 2003). The deformation pattern of the ATF system depends on how strain associated with India–Eurasia convergence has been partitioned. One perspective argues that the ATF exhibits left-slip motion and the NAF experiences thrust/reverse slip with limited left-slip of <30 km (Yue & Liou, 1999; Yue et al., 2004). On the other hand, the NAF was regarded as a primary strike-slip fault with an offset of 120 km (Cowgill et al., 2000, 2003; Yin et al., 2002). Recent studies suggest a mid-Miocene tectonic reorganization when the NAF transitioned from a left-lateral fault to a reverse-slip fault (S. Gao et al., 2022; L. Wu et al., 2019). Indeed,

Writing – review & editing:
Chenglong Wu, Tao Xu, Ross N. Mitchell, Jianfeng Yang

a better understanding of the spatial and temporal evolution of deep structures throughout the ATF system could greatly enhance our comprehension of how the continental lithosphere reacts to the far-field continental collision.

Quite a few geophysical observations suggest that the Tarim continental lithosphere is underthrusting beneath the ATR, but the patterns vary in underthrusting depth and polarity (R. Gao et al., 2001; Shi et al., 2007; Wittlinger et al., 1998; L. Zhang et al., 2015; J. Zhao et al., 2006). Teleseismic tomography suggests that the whole Tarim crust plunges steeply southward beneath the ATF to 150 km depth (Wittlinger et al., 1998), supported also by magnetotellurics (MT) observations (L. Zhang et al., 2015), suggesting the ATF is a through-going lithospheric fault. However, the results from a wide-angle reflection profile propose southwestward underthrusting of the Tarim lithosphere below the ATR and viewed ATF as an intracrustal fault (J. Zhao et al., 2006).

Geodynamic modeling suggests that the crustal rheological heterogeneity governed the intracontinental deformation of the Tibetan margin (L. Chen et al., 2017; R. Xie et al., 2023; J. Yang et al., 2020). The intracontinental deformation of the ATR was closely correlated to the crustal structures and relative strengths of the eastern Tarim Basin (ETB) and western Qaidam Basin (WQB) located on both sides of the ATR. The Precambrian basement of Tarim comprises continental blocks that assembled in the Paleoproterozoic (H. Yang et al., 2018). Cenozoic strata exhibit negligible deformation (Laborde et al., 2019). The most significant event that impacted the Tarim basement during the Phanerozoic was an early Permian mantle plume which strengthened the Tarim lithosphere (X. Xu et al., 2021; Y.-G. Xu et al., 2014), despite some controversy surrounding the existence of mantle plumes. The Qaidam Basin, the largest Cenozoic sedimentary basin of the plateau, formed on the Proterozoic–Paleozoic basement, and numerous active reverse faults bound the basin to the north and south, implying N–S shortening related to the India–Eurasia continental collision (Y. Wang et al., 2012). Some geophysical studies suggest the existence of lower-crustal flow beneath the western basin (L. Zhang et al., 2015; J. Zhao et al., 2006), however, such a model contradicts the crust-mantle coupling deformation indicated by SKS splitting measurements (Chang & Wang, 2023).

Here, we used the *P*-wave Receiver function (RF) technique to investigate the fine crustal structure across the central ATF. The deployed NW–SE oriented dense array crosses the ETB, ATR, and WQB, separated by the NAF and ATF, respectively. Our observations shed new light on the intracontinental deformation pattern across the northern edge of the Tibetan Plateau.

2. Data and Methods

A generally NW–SE-trending dense seismic array was employed across the northern boundary of the Tibetan Plateau from September 2021 to November 2021 (Figure 1, T. Xie et al., 2023). The array consisted of 475 short-period seismic stations along a ∼430-km long cross-section with a ∼0.9-km station spacing. We selected well-recorded teleseismic events with Mw ≥ 5.5 at epicentral distances from 28 to 95°. After rotating the waveforms from the ZNE to the ZRT coordinate system, we calculated radial RFs by applying the time-domain iterative deconvolution technique (Ligorría & Ammon, 1999) with a Gaussian parameter of 5.0. Upon removing low-quality RFs through visual inspection, a collection of 7,013 RFs from 41 events was obtained, offering satisfactory coverage in both azimuth and distance aspects (Figure 1, Figure S1 in Supporting Information S1).

We employed the Common Conversion Point (CCP) stacking technique (Zhu, 2000) to obtain the crustal structure under the seismic array (Figure 2c; See Text S1 in Supporting Information S1). The reference velocity model for migration was based on the wide-angle reflection profile (J. Zhao et al., 2006), and varying Vp/Vs ratios were determined with the *H*–κ method (Table S1 in Supporting Information S1). All amplitudes were projected orthogonally onto the reference profile (green line in Figure 1) to generate the CCP image. The *H*–κ stacking approach was utilized to estimate crustal thickness (*H*) and bulk Vp/Vs ratio (κ) (Zhu & Kanamori, 2000) (Text S2 and Figures S2–S5 in Supporting Information S1). A cluster of RFs within a range of 21 stations were collected at the center station and were analyzed with the *H*–κ method, and the center stations were shifted in increments of 10 stations (Figure 2, Table S2 in Supporting Information S1).

A two-dimensional hybrid numerical approach (Y. Liu et al., 2013, 2014, 2017; L. Zhao et al., 2008) was used to generate the synthetic seismograms for various crustal structures (Text S3 in Supporting Information S1). The crustal velocity model (Figure 3c) was designed based on the interpreted CCP image (Figure 2c) and the velocity model from the wide-angle profile (J. Zhao et al., 2006). Then, we computed the radial RFs and conducted the

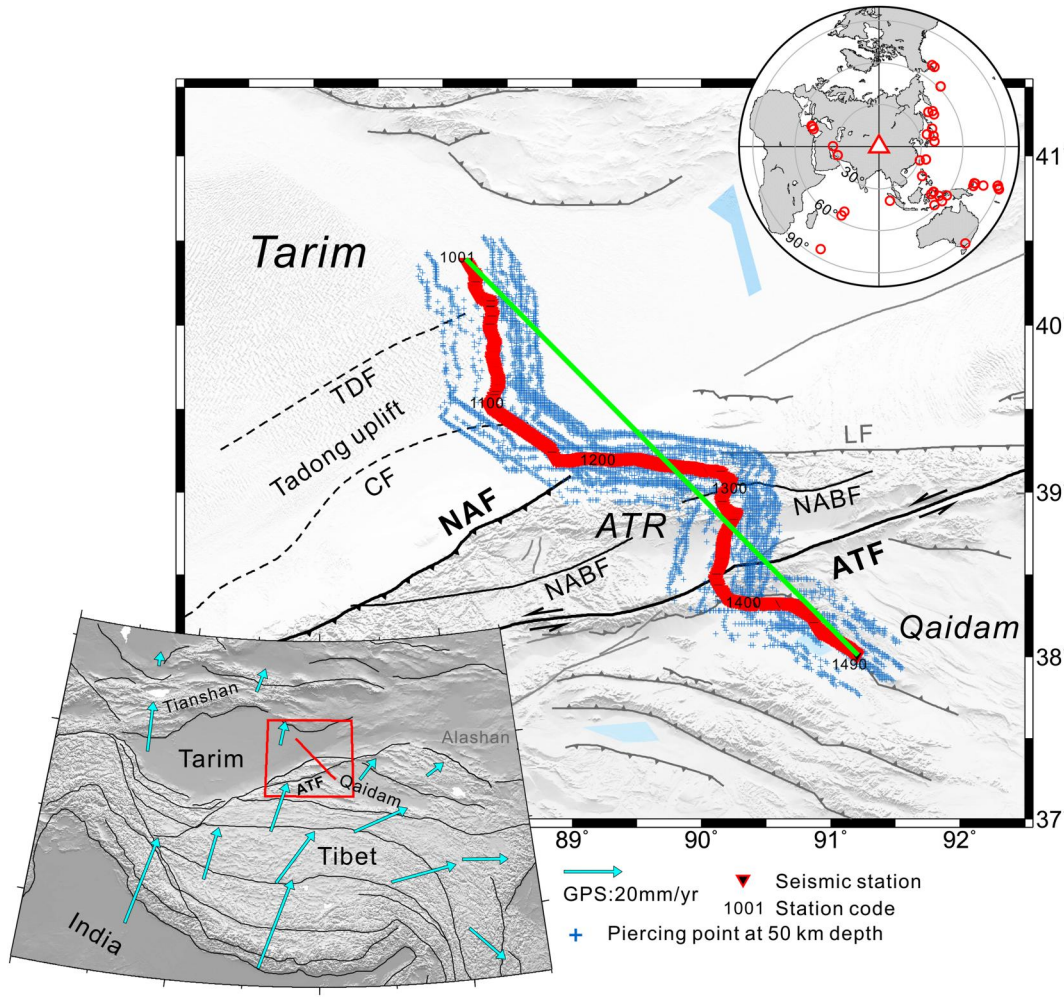

Figure 1. Tectonic setting of the Altyn Tagh Range and location of the dense seismic array. The red triangles indicate the dense array with the numbers representing the reference station codes, and the green line shows the imaging profile. Black and gray solid lines represent the main faults. The black dashed lines are inherited but non-reactivated faults. The blue crosses show the piercing points at 50 km depth for Ps conversions. The upper-right inset shows the employed earthquake events. The lower-left inset is the map of the Tibetan Plateau and surrounding tectonic units. The red box and the red line denote the study region and the seismic array, respectively. Those light-blue arrows show the average GPS velocity field (D. Wang et al., 2020). TDF: Tadong Fault; CF: Cherchen fault; NAF: North Altyn Fault; NABF: North Altyn Branch Fault; LF: Lapeiquan Fault; ATR: Altyn Tagh Range; and ATF: Altyn Tagh Fault.

CCP stacking method utilizing the identical deconvolution algorithm, migration technique, and parameters as those used for the real data set (Figure 3d).

3. Results

Limited events recorded by some stations in the WQB restricted the CCP imaging (Figures S1 in Supporting Information S1), and there are four possible scenarios for tectonic interpretation based on the CCP image (Figure 2c). Through synthetic tests and CCP imaging with different Gaussian parameters, three scenarios can be ruled out (Figures S6–S9 and Text S4 in Supporting Information S1). Finally, we tend to support the current scenario (Figure 2c).

Various approaches were used to establish the reliability of the findings. First, most bins of the CCP volume have more than 100 stacked RFs (Figure S10 in Supporting Information S1), ensuring an adequate sampling size for CCP imaging. Second, we constructed the crustal structure image by CCP stacking of the PpPs multiples (Figure S11 in Supporting Information S1). The consistency of the interpreted interfaces produced from the PpPs and Ps

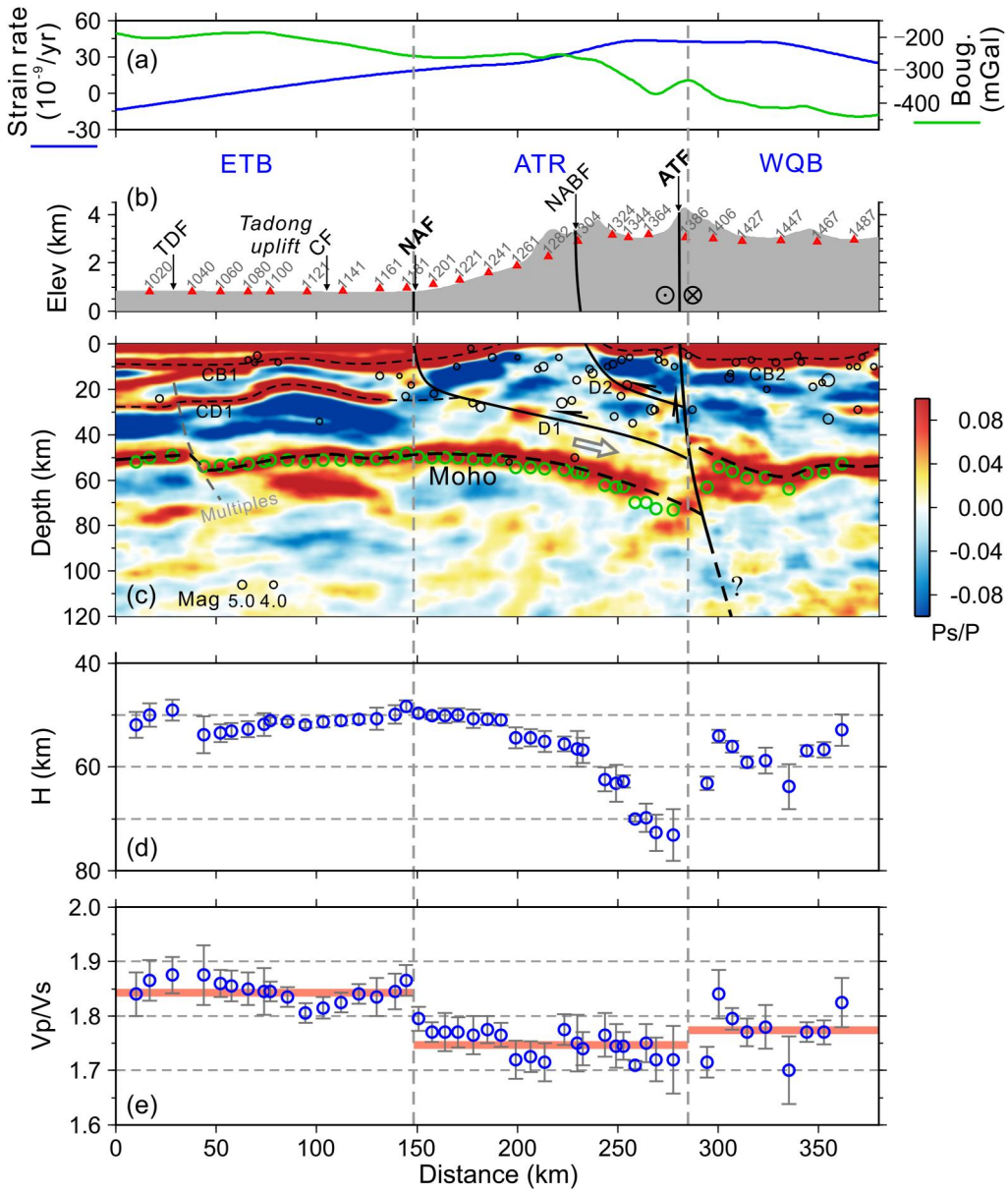

Figure 2. Comprehensive geophysical observations along the profile. (a) Strain rates and Bouguer gravity observations across the Altyn Tagh Range (ATR) (Kreemer et al., 2014; Pavlis et al., 2012). (b) The station locations (red triangles) with a spacing of 20 stations and surface topography along the profile. The study region is divided into three tectonic units including eastern Tarim Basin, ATR, and western Qaidam Basin, separated by North Altyn Fault (NAF) and Altyn Tagh Fault, respectively. (c) Common Conversion Point image. The interpreted interfaces include crystalline basement (CB1 and CB2), Conrad discontinuity CD1, the faults NAF and NABF (D1 and D2), and the Moho. The black circles denote the earthquakes with magnitudes greater than 3.0 that occurred between 1977 and 2012, and these earthquakes are within 80 km from the migrated profile. (d) Crustal thickness at the center stations (see Section 2. Data and Methods) estimated by *H*–κ stacking approach (blue circles), also denoted by the green circles in panel (b). (e) Vp/Vs ratios derived from *H*–κ stacking approach (blue circles). The mean Vp/Vs ratios for the three tectonic units are shown by the pink solid lines.

phases suggests that the CCP images are reliable and the Vp/Vs ratios are adequate. Furthermore, additional tests including bootstrap resampling, event back-azimuths, and stacking bins confirm that the crustal structure image is robust (Figures S10, S12, and S13 in Supporting Information S1). In addition, to mitigate the impact of the tortuosity of the profile on CCP imaging, we conducted segmented CCP imaging for four sections along the survey line and obtained a crustal structure that is almost identical to that in Figure 2c (Figure S14 in Supporting Information S1). Finally, the strong agreement between the observed and synthetic CCP images validates the

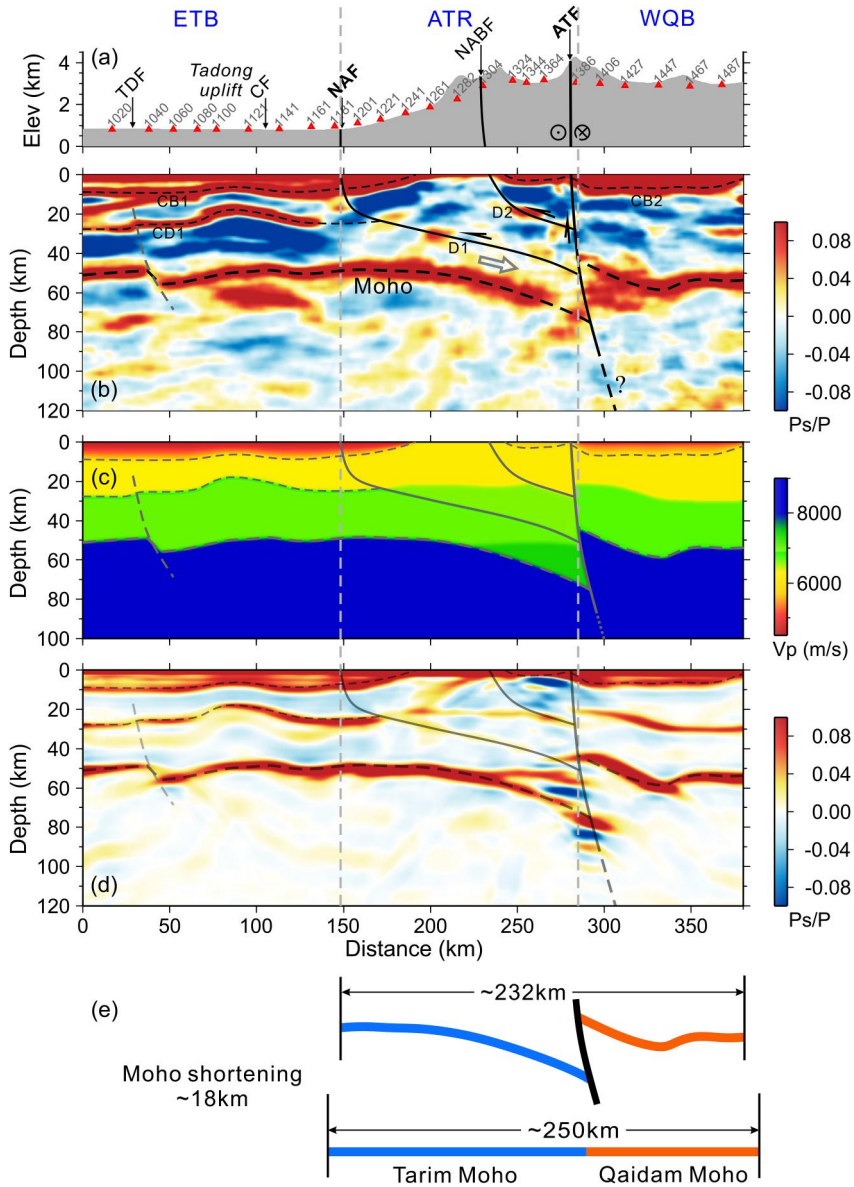

Figure 3. Comparison of the observed and synthetic migrated images and balanced cross-section across the Altyn Tagh Range (ATR). (a) The station locations (red triangles) with a spacing of 20 stations and surface topography along the profile. (b) Migrated Ps image of the crustal structure, same as Figure 2c. (c) Two-dimensional Vp velocity model constructed based on panel (b). (d) Synthetic Common Conversion Point image for the preferred velocity model (c). The light gray lines in panels (c, d) are identical to the black lines in panel (b). (e) Estimation of the Cenozoic crustal shortening across the ATR based on the balanced cross-section of Moho length.

interpreted crustal structure as reliable interfaces (Figure 3). Comparison with previous geophysical observations also supports the underthrusting of the Tarim lower crust beneath the Tibetan Plateau (Text S5 and Figure S15 in Supporting Information S1).

The dense array reveals the fine crustal structure across the ATR. Predominant positive conversions at the depths of 50–75 km are recognized as signals of the Moho (Figure 2c), which also can be identified at 6–9 s in the time-domain stacked RFs (Figure S1 in Supporting Information S1). Based on the Moho undulation and the regional tectonics, the CCP image is partitioned into three segments: ETB, ATR, and WQB, divided by the NAF and the ATF, respectively. Our CCP image shows that the Moho below the ETB remains at ~50 km, consistent with the results from wide-angle reflection (J. Zhao et al., 2006). Moreover, the image also clearly reveals a prominent

Moho offset of ∼5 km under the Tadong Fault (TF). The Moho beneath the ATR deepens to the southeast and reaches 75 km depth under the ATF. Beneath the WQB, the Moho increases from 45 to 59 km, then decreases to 54 km (Figure 2c).

Some intracrustal signals are also recognized in the Ps image. The CB1 signal, positive conversions at 6–9 km depth under the ETB, likely represents the crystalline basement. CB1 bulges upwards from 9 to 6 km, which is also recognized as the Tadong uplift by the prospecting reflection profile (H. Liu et al., 2016). The CD1 signal is the Conrad discontinuity under the ETB corresponding to the continuous positive conversions at 18–28 km depth. The two intermittent southeast-dipping interfaces D1 and D2 under the ATR could be traced to the NAF and NABF. They are regarded as the deeper segments of the two faults, respectively. The seismicity appears to be distributed along the two southeast-dipping listric faults (Figure 2c). The CB2 signal, the positive amplitudes at ∼7 km depth under the WQB, likely represents the crystalline basement.

Apart from the large lateral undulation under the complicated ATF, the Moho geometry in the CCP image coincides well with the crustal thickness estimated by H–κ stacking (Figure 2c). The consistency improves the dependability of the varying crustal Vp/Vs ratios (Figure 2e). The ETB is featured by the highest bulk Vp/Vs ratios spanning from 1.80 to 1.88 with an average of 1.84. In comparison, the ATR stands out for the lowest Vp/Vs ratios (1.71–1.78 with an average of 1.75). The WQB exhibits some variations of Vp/Vs ratios from 1.70 to 1.83, averaging at 1.77 (Figure 2e).

4. Discussion

4.1. Strengthening the Ancient Crust of Tarim by Plume Activity

The horizontally layered Cenozoic strata suggests negligible deformation in the Tarim Basin (Laborde et al., 2019). The ETB crustal structure, including the Moho offset and upward convexity of CB1 and CD1, preserves remnants of major tectonic events prior to the Cenozoic. The Moho offset beneath the TF is located within the Central Tarim Terrain (CTT), delineated by an increased aeromagnetic anomaly along 40°N latitude, which separates the Northern and Southern Tarim Terranes (W.-C. Yang et al., 2012). Extensive magmatic activity at ca. 1.9 Ga indicates that the CTT represents a Paleoproterozoic orogenic belt formed by the amalgamation of the two terranes (H. Yang et al., 2018). The spatial correlation suggests that the inherited and non-reactivated TF functions as the Tarim suture zone. The CB1, also known as the Tadong uplift, is one of the major ancient uplifts within Tarim. A comprehensive analysis indicates that the most intense deformation in the Paleozoic occurred in the middle Devonian, which led to the uplifts of CB1 and CD1 (Lin et al., 2012). The Tianshan–Tarim collision is considered the main factor responsible for the deformation within the Tadong uplift (Lin et al., 2012).

The high Vp/Vs value of 1.84 (Figure 2e), along with low heat flow (Jiang et al., 2019), high Vp in the mid-lower crust (J. Zhao et al., 2006), and high resistivity (L. Zhang et al., 2015), indicates mafic/ultramafic compositions in the crust of the ETB, even considering the sedimentary layer (see Text S6 in Supporting Information S1). Widespread igneous activity in the Tarim Basin during the early Permian formed a large igneous province, presumably triggered by a mantle plume (Y.-G. Xu et al., 2014). A thermal pulse related to the plume impacted most of the Tarim Basin (X. Xu et al., 2021). The interactions between the plume and lithosphere reinforced Tarim into a stable cratonic continent by intruding mafic rocks into the lower crust (Deng et al., 2017; X. Xu et al., 2021). The process led to the high Vp/Vs ratios observed in the ETB. Additionally, being a pre-existing structurally suture zone, the crust beneath the TF might have experienced Moho uplift during plume activity, contributing to the currently notably Moho offset of ∼5 km.

4.2. Underthrusting of Tarim Lower Crust Beneath Tibetan Plateau

The most striking feature in our CCP image is that the Moho gradually deepens southeastward from 50 to 75 km, terminating beneath the ATF. This observation does not support the idea that the underthrust crust exceeds 100 km depth (Wittlinger et al., 1998; L. Zhang et al., 2015). The continuously traceable Moho signals and an obvious Moho offset beneath the ATF appear to contradict the southwestward underthrusting of the Tarim lower crust (J. Zhao et al., 2006). The dipping Moho combined with D1 (NAF) delineates the underthrusting of the Tarim lower crust under the ATR. Thus, the NAF is a reverse-dominated fault, which is corroborated by sedimentary evidence (Yue et al., 2004). The NW–SE oriented two-dimensional array may not fully capture the complex three-dimensional structure. By combining the N–S oriented GPS observations in the ETB and

10.1029/2024GL108220

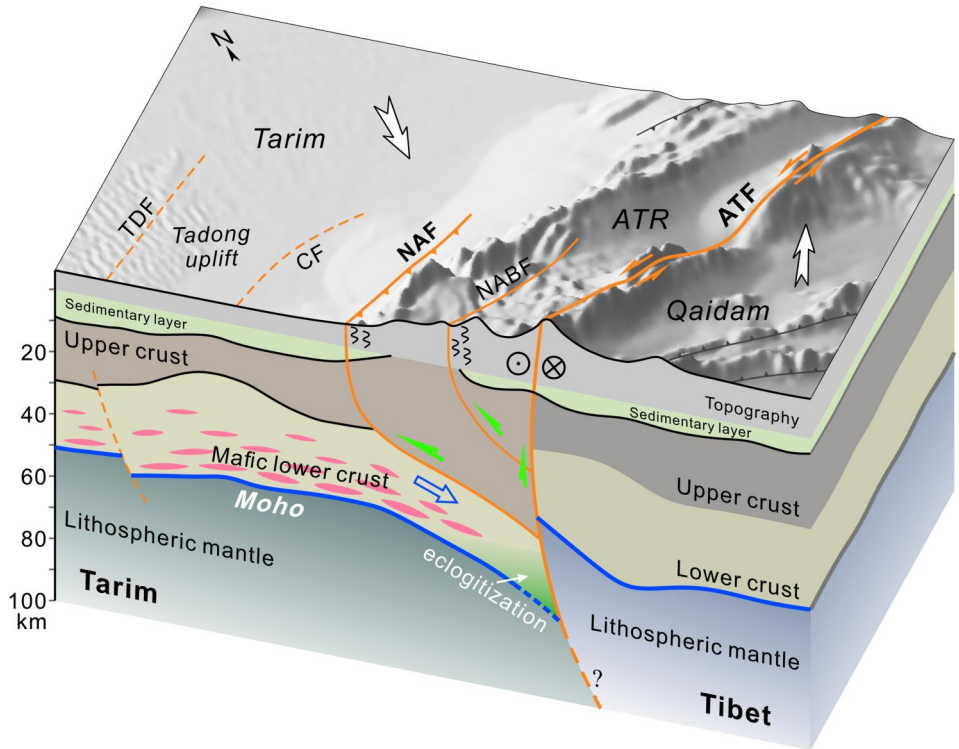

Figure 4. Cartoon for Tarim lower crust underthrusting beneath the Tibetan Plateau. The interpreted interfaces were based on the Common Conversion Point image (Figure 2c). The white arrows are the directions of relative motion indicated by GPS observations. The mafic Tarim lower crust is underthrusting to ~75 km beneath the Tibet Plateau, and the underthrusting wedge experienced partial eclogitization. Oblique convergent forces extruded upper crustal materials along the two faults North Altyn Fault and NABF, generating the pop-up structure of Altyn Tagh Range.

clockwise rotation of the Tarim Block (J. Zhao et al., 2019), we inferred that the Tarim lower crust is likely underthrusting southward beneath the ATF. The ATR experienced transpressive deformation as a result of the oblique convergence between the Tarim and Qaidam. In contrast to the lower crust modified by mantle plume activity, the weaker upper crustal materials were extruded upward along the thrusts D1 and D2 due to oblique convergent forces, leading to the formation of the pop-up structure (Figure 4). The pop-up structures refers to uplifted blocks or topography formed by compression between thrusts and reverse faults that have opposing vergence, or at restraining bends and stepovers on strike-slip faults. One common scenario leading to the formation of pop-up structures is during the collision of tectonic plates, such as in this study region. The upper-crustal thickening induced the bulk felsic composition, suggested by the average Vp/Vs value of 1.75 for ATR (Figure 2e). The intense deformation in the upper crust resulted in stronger seismicity of the ATR compared to the surrounding blocks (Figure 2c), substantiated by the elevated strain rate (Figure 2a).

The underthrusting root zone, which extends from 50 to 75 km depth, is featured by an elevated Bouguer gravity anomaly (Figure 2a), a wedge-shaped low-velocity of 7.3–7.8 km/s (J. Zhao et al., 2006) and a high-density anomaly of 40 kg/m^3 (Deng et al., 2017). These observations suggest that the lower crust is probably partially eclogitized. The seismic properties of eclogite, which resemble those of peridotite in the upper mantle, result in weaker Moho conversions under the ATF (Figure 2c). The presence of a Moho offset of ~30 km demonstrates that the ATF cuts through the entire crust. The nearly vertical ATF slightly dips southeastward in the deep section. The deep shear zone along the fault, resembling the metamorphic mylonite belt (Wittlinger et al., 1998), serves as a barrier, preventing the underthrusting of the Tarim lower crust (Figure 4).

The underthrusting process caused the uplift of the Qaidam Moho to 45 km depth. The mean Vp/Vs value for the WQB is a moderate value of 1.77, reflecting intermediate crustal compositions (Christensen, 1996). The Vp/Vs ratios at most stations for the WQB are too low to substantiate the presence of a crustal flow layer (L. Zhang et al., 2015), which would increase Vp/Vs ratio to at least 1.80 (Z. Liu et al., 2021). The NNE-oriented

compressional stress field created the WNW–ESE-trending thrusts and the strike-parallel fast directions, indicating that the crust-mantle coupling deformation in the WQB (Chang & Wang, 2023).

4.3. Onset of Altyn Tagh Range Uplift

Due to the early Cenozoic peneplanation in northern Tibet (Liu-Zeng et al., 2008), the Moho undulation in the CCP image can serve as a crucial marker for estimating the shortening across the ATR in response to the Cenozoic India–Eurasia collision. The Moho under the ATR and WQB was assumed to be flat prior to the Cenozoic. Based on the balanced cross-section technique (Li et al., 2016), we summed the lengths of each Moho section and estimated the NW–SE pre-deformation width of the target area to be ∼250 km. This suggests NW–SE shortening of ∼18 km when comparing with the present width of ∼232 km (Figure 3e), consistent with the shortening of 24 ± 9 km by structural restorations (Laborde et al., 2019). The shortening rate perpendicular to the NAF is estimated to be 2–4 mm/yr according to reconnaissance of fault scarps (Molnar et al., 1987), velocity models for the India–Eurasia collision region (Peltzer & Saucier, 1996), as well as GPS velocities projected along NW–SE orientation (D. Wang et al., 2020). Thus, we can infer that the significant shortening commenced at ca. 9–5 Ma. Since the pop-up structure of the upper crust has also absorbed some deformation, the estimated time may represent a lower limit. The starting time aligns approximately with the onset of rapid uplift of the ATR (late Miocene, ca. 10 Ma), based on sedimentology (Song et al., 2019), thermochronology (Z.-L. Chen et al., 2006), and other methods (T. Zhang et al., 2016). Therefore, the ductile deformation in the lower crust coincides well with the pop-up structure in the upper crust, and with geomorphic and geodesic observations, supporting the notion that there was an intensification of intracontinental deformation in the ATR since the late Miocene.

5. Conclusion

We obtained a detailed crustal structure across the central ATF by RF method using the data from a dense array. The image indicates that the Tarim lower crust is underthrusting beneath the Tibetan Plateau to ∼75 km depth. Oblique convergent forces has caused the uplift of the ATR since the late Miocene.

Data Availability Statement

The receiver functions used in this study are available at C. Wu et al. (2023). The hk1.3 software package (Zhu, 2009) is used for calculating receiver functions and conducting H–κ stacking. The ccp1.0 codes (Zhu, 2009) are used for CCP stacking of receiver functions.

Acknowledgments
The authors are grateful to Geophysical Exploration Center, China Earthquake Administration for the field data acquisition. We appreciate the support by Dr. Youshan Liu in the forward modeling. We thank Profs. Ling Chen, Qingren Meng, and Laicheng Miao for constructive discussions. The work was financially supported by the Second Tibetan Plateau Scientific Expedition and Research Program (STEP, 2019QZKK0701-02), K. C. Wong Education Foundation (GJTD-2019-04), and the National Natural Science Foundation of China (Grant 42030308, 42130807, and 42104102).

References

Chang, L., & Wang, C. (2023). Teleseismic shear wave splitting and intracontinental collision deformation of the northern Tibetan Plateau and the eastern Tarim basin. *Science China Earth Sciences*, *66*(7), 1–13. https://doi.org/10.1007/s11430-022-1068-5

Chen, L., Capitanio, F. A., Liu, L., & Gerya, T. V. (2017). Crustal rheology controls on the Tibetan plateau formation during India-Asia convergence. *Nature Communications*, *8*(1), 15992. https://doi.org/10.1038/ncomms15992

Chen, Z.-L., Gong, H.-L., & Li, L. (2006). Cenozoic uplifting and exhumation process of the Altyn Tagh mountains. *Earth Science Frontiers*, *13*(4), 91.

Christensen, N. I. (1996). Poisson's ratio and crustal seismology. *Journal of Geophysical Research*, *101*(B2), 3139–3156. https://doi.org/10.1029/95jb03446

Cowgill, E., Yin, A., Feng, W. X., & Qing, Z. (2000). Is the North Altyn fault part of a strike-slip duplex along the Altyn Tagh fault system? *Geology*, *28*(3), 255–258. https://doi.org/10.1130/0091-7613(2000)028<0255:itnafp>2.3.co;2

Cowgill, E., Yin, A., Harrison, T. M., & Wang, X. (2003). Reconstruction of the Altyn Tagh fault based on U-Pb geochronology: Role of back thrusts, mantle sutures, and heterogeneous crustal strength in forming the Tibetan Plateau. *Journal of Geophysical Research*, *108*(B7), 2346. https://doi.org/10.1029/2002jb002080

Deng, Y., Levandowski, W., & Kusky, T. (2017). Lithospheric density structure beneath the Tarim basin and surroundings, northwestern China, from the joint inversion of gravity and topography. *Earth and Planetary Science Letters*, *460*, 244–254. https://doi.org/10.1016/j.epsl.2016.10.051

Gao, R., Li, P., Li, Q., Guan, Y., Shi, D., Kong, X., & Liu, H. (2001). Deep process of the collision and deformation on the northern margin of the Tibetan Plateau: Revelation from investigation of the deep seismic profiles. *Science in China - Series D: Earth Sciences*, *44*(S1), 71–78. https://doi.org/10.1007/bf02911973

Gao, S., Cowgill, E., Wu, L., Lin, X., Cheng, X., Yang, R., et al. (2022). From left slip to transpression: Cenozoic tectonic evolution of the North Altyn Fault, NW margin of the Tibetan Plateau. *Tectonics*, *41*(3), e2021TC006962. https://doi.org/10.1029/2021tc006962

Hu, X., Wu, L., Zhang, Y., Zhang, J., Wang, C., Tang, J., et al. (2022). Multiscale lithospheric buckling dominates the Cenozoic subsidence and deformation of the Qaidam Basin: A new model for the growth of the northern Tibetan Plateau. *Earth-Science Reviews*, *234*, 104201. https://doi.org/10.1016/j.earscirev.2022.104201

Jiang, G., Hu, S., Shi, Y., Zhang, C., Wang, Z., & Hu, D. (2019). Terrestrial heat flow of continental China: Updated dataset and tectonic implications. *Tectonophysics*, *753*, 36–48. https://doi.org/10.1016/j.tecto.2019.01.006

Kreemer, C., Blewitt, G., & Klein, E. C. (2014). A geodetic plate motion and global strain rate model. *Geochemistry, Geophysics, Geosystems*, *15*(10), 3849–3889. https://doi.org/10.1002/2014gc005407

Laborde, A., Barrier, L., Simoes, M., Li, H., Coudroy, T., van Der Woerd, J., & Tapponnier, P. (2019). Cenozoic deformation of the Tarim Basin and surrounding ranges (Xinjiang, China): A regional overview. *Earth-Science Reviews*, *197*, 102891. https://doi.org/10.1016/j.earscirev.2019.102891

Li, J., Zhang, J., Zhao, X., Jiang, M., Li, Y., Zhu, Z., et al. (2016). Mantle subduction and uplift of intracontinental mountains: A case study from the Chinese Tianshan Mountains within Eurasia. *Scientific Reports*, *6*(1), 28831. https://doi.org/10.1038/srep28831

Ligorría, J. P., & Ammon, C. J. (1999). Iterative deconvolution and receiver-function estimation. *Bulletin of the Seismological Society of America*, *89*(5), 1395–1400. https://doi.org/10.1785/bssa0890051395

Lin, C., Yang, H., Liu, J., Rui, Z., Cai, Z., & Zhu, Y. (2012). Distribution and erosion of the Paleozoic tectonic unconformities in the Tarim Basin, Northwest China: Significance for the evolution of paleo-uplifts and tectonic geography during deformation. *Journal of Asian Earth Sciences*, *46*, 1–19. https://doi.org/10.1016/j.jseaes.2011.10.004

Liu, H., Somerville, I. D., Lin, C., & Zuo, S. (2016). Distribution of Palaeozoic tectonic superimposed unconformities in the Tarim Basin, NW China: Significance for the evolution of palaeogeomorphology and sedimentary response. *Geological Journal*, *51*(4), 627–651. https://doi.org/10.1002/gj.2664

Liu, Y., Teng, J., Lan, H., Si, X., & Ma, X. (2014). A comparative study of finite element and spectral element methods in seismic wavefield modeling. *Geophysics*, *79*(2), T91–T104. https://doi.org/10.1190/geo2013-0018.1

Liu, Y., Teng, J., Liu, S., & Xu, T. (2013). Explicit finite element method with triangle meshes stored by sparse format and its perfectly matched layers absorbing boundary condition. *Chinese Journal of Geophysics*, *56*(9), 3085–3099.

Liu, Y., Teng, J., Xu, T., & Badal, J. (2017). Higher-order triangular spectral element method with optimized cubature points for seismic wavefield modeling. *Journal of Computational Physics*, *336*, 458–480. https://doi.org/10.1016/j.jcp.2017.01.069

Liu, Z., Tian, X., Liang, X., Liang, C., & Li, X. (2021). Magmatic underplating thickening of the crust of the southern Tibetan Plateau inferred from receiver function analysis. *Geophysical Research Letters*, *48*(17), e2021GL093754. https://doi.org/10.1029/2021gl093754

Liu-Zeng, J., Tapponnier, P., Gaudemer, Y., & Ding, L. (2008). Quantifying landscape differences across the Tibetan Plateau: Implications for topographic relief evolution. *Journal of Geophysical Research*, *113*(F4), F04018. https://doi.org/10.1029/2007jf000897

Molnar, P., Burchfiel, B. C., Liang, K., & Zhao, Z. (1987). Geomorphic evidence for active faulting in the Altyn Tagh and northern Tibet and qualitative estimates of its contribution to the convergence of India and Eurasia. *Geology*, *15*(3), 249–253. https://doi.org/10.1130/0091-7613(1987)15<249:gefafi>2.0.co;2

Molnar, P., & Dayem, K. E. (2010). Major intracontinental strike-slip faults and contrasts in lithospheric strength. *Geosphere*, *6*(4), 444–467. https://doi.org/10.1130/ges00519.1

Pavlis, N. K., Holmes, S. A., Kenyon, S. C., & Factor, J. K. (2012). The development and evaluation of the Earth gravitational Model 2008 (EGM2008). *Journal of Geophysical Research*, *117*(B4), B04406. https://doi.org/10.1029/2011jb008916

Peltzer, G., & Saucier, F. (1996). Present-day kinematics of Asia derived from geologic fault rates. *Journal of Geophysical Research*, *101*(B12), 27943–27956. https://doi.org/10.1029/96jb02698

Shi, D., Yu, Q., Poupinet, G., Herquel, G., Wittlinger, G., & Jiang, M. (2007). Crustal structures across the Altyn Tagh fault imaged by teleseismic receiver functions and their geodynamic implications. *Acta Geologica Sinica*, *81*(1), 139–144. (in Chinese).

Song, X., Cheng, X., Lin, X., & Gao, S. (2019). Cenozoic tectonic evolution of the Altyn Tagh: Evidence from sedimentary record in Ruoqiang depression of the southeastern Tarim Basin. *Chinese Journal of Geology*, *54*(2), 330–344. https://doi.org/10.12017/dzkx.2019.020

Tapponnier, P., Zhiqin, X., Roger, F., Meyer, B., Arnaud, N., Wittlinger, G., & Jingsui, Y. (2001). Oblique stepwise rise and growth of the Tibet Plateau. *Science*, *294*(5547), 1671–1677. https://doi.org/10.1126/science.105978

Tian, X., Bai, Z., Klemperer, S. L., Liang, X., Liu, Z., Wang, X., et al. (2021). Crustal-scale wedge tectonics at the narrow boundary between the Tibetan Plateau and Ordos block. *Earth and Planetary Science Letters*, *554*, 116700. https://doi.org/10.1016/j.epsl.2020.116700

Wang, D., Zhao, B., Yu, J., & Tan, K. (2020). Active tectonic deformation around the Tarim Basin inferred from dense GPS measurements. *Geodesy and Geodynamics*, *11*(6), 418–425. https://doi.org/10.1016/j.geog.2020.09.001

Wang, Y., Zheng, J., Zhang, W., Li, S., Liu, X., Yang, X., & Liu, Y. (2012). Cenozoic uplift of the Tibetan Plateau: Evidence from the tectonic–sedimentary evolution of the western Qaidam Basin. *Geoscience Frontiers*, *3*(2), 175–187. https://doi.org/10.1016/j.gsf.2011.11.005

Wittlinger, G., Tapponnier, P., Poupinet, G., Mei, J., Danian, S., Herquel, G., & Masson, F. (1998). Tomographic evidence for localized lithospheric shear along the Altyn Tagh fault. *Science*, *282*(5386), 74–76. https://doi.org/10.1126/science.282.5386.74

Wu, C., Xu, T., Tian, X., Mitchell, R., Lin, J., Yang, J., et al. (2023). Receiver function data obtained from the dense seismic profile across the central Altyn Tagh range [Dataset]. WDC for Geophysics. https://doi.org/10.12197/2023GA014

Wu, L., Lin, X., Cowgill, E., Xiao, A., Cheng, X., Chen, H., et al. (2019). Middle Miocene reorganization of the Altyn Tagh fault system, northern Tibetan Plateau. *Bulletin*, *131*(7–8), 1157–1178. https://doi.org/10.1130/b31875.1

Xie, R., Chen, L., Yin, A., Xiong, X., Chen, Y. J., Guo, Z., & Wang, K. (2023). Two phases of crustal shortening in northeastern Tibet as a result of a stronger Qaidam lithosphere during the Cenozoic India–Asia collision. *Tectonics*, *42*(1), e2022TC007261. https://doi.org/10.1029/2022tc007261

Xie, T., Xu, T., Yang, Y., Tian, X., Lin, J., Wu, C., & Lu, Z. (2023). Observation of higher-mode Rayleigh waves from ambient noise in the Tarim Basin, China. *Seismological Research Letters*, *94*(4), 1848–1859. https://doi.org/10.1785/0220220361

Xu, X., Zuza, A. V., Yin, A., Lin, X., Chen, H., & Yang, S. (2021). Permian plume-strengthened Tarim lithosphere controls the Cenozoic deformation pattern of the Himalayan-Tibetan orogen. *Geology*, *49*(1), 96–100. https://doi.org/10.1130/g47961.1

Xu, Y.-G., Wei, X., Luo, Z.-Y., Liu, H.-Q., & Cao, J. (2014). The early permian Tarim large igneous province: Main characteristics and a plume incubation model. *Lithos*, *204*, 20–35. https://doi.org/10.1016/j.lithos.2014.02.015

Yang, H., Wu, G., Kusky, T. M., Chen, Y., & Xiao, Y. (2018). Paleoproterozoic assembly of the North and South Tarim terranes: New insights from deep seismic profiles and Precambrian granite cores. *Precambrian Research*, *305*, 151–165. https://doi.org/10.1016/j.precamres.2017.11.015

Yang, J., Kaus, B. J., Li, Y., Leloup, P. H., Popov, A. A., Lu, G., et al. (2020). Lower crustal rheology controls the development of large offset strike-slip faults during the Himalayan-Tibetan orogeny. *Geophysical Research Letters*, *47*(18), e2020GL089435. https://doi.org/10.1029/2020gl089435

Yang, W.-C., Wang, J.-L., Zhong, H.-Z., & Chen, B. (2012). Analysis of regional magnetic field and source structure in Tarim Basin. *Chinese Journal of Geophysics*, *55*(4), 1278–1287. https://doi.org/10.6038/j.issn.0001-5733.2012.04.023

Yin, A., & Harrison, T. M. (2000). Geologic evolution of the Himalayan-Tibetan orogen. *Annual Review of Earth and Planetary Sciences*, *28*(1), 211–280. https://doi.org/10.1146/annurev.earth.28.1.211

Yin, A., Rumelhart, P., Butler, R., Cowgill, E., Harrison, T., Foster, D., et al. (2002). Tectonic history of the Altyn Tagh fault system in northern Tibet inferred from Cenozoic sedimentation. *Geological Society of America Bulletin*, *114*(10), 1257–1295. https://doi.org/10.1130/0016-7606(2002)114<1257:thotat>2.0.co;2

Yue, Y., & Liou, J. G. (1999). Two-stage evolution model for the Altyn Tagh fault, China. *Geology*, *27*(3), 227–230. https://doi.org/10.1130/0091-7613(1999)027<0227:tsemft>2.3.co;2

Yue, Y., Ritts, B. D., Graham, S. A., Wooden, J. L., Gehrels, G. E., & Zhang, Z. (2004). Slowing extrusion tectonics: Lowered estimate of post-early Miocene slip rate for the Altyn Tagh Fault. *Earth and Planetary Science Letters*, *217*(1–2), 111–122. https://doi.org/10.1016/s0012-821x(03)00544-2

Zhang, L., Unsworth, M., Jin, S., Wei, W., Ye, G., Jones, A. G., et al. (2015). Structure of the Central Altyn Tagh Fault revealed by magnetotelluric data: New insights into the structure of the northern margin of the India–Asia collision. *Earth and Planetary Science Letters*, *415*, 67–79. https://doi.org/10.1016/j.epsl.2015.01.025

Zhang, T., Han, W., Fang, X., Zhang, W., Song, C., & Yan, M. (2016). Intensified tectonic deformation and uplift of the Altyn Tagh range recorded by rock magnetism and growth strata studies of the western Qaidam Basin, NE Tibetan Plateau. *Global and Planetary Change*, *137*, 54–68. https://doi.org/10.1016/j.gloplacha.2015.12.017

Zhao, J., Mooney, W. D., Zhang, X., Li, Z., Jin, Z., & Okaya, N. (2006). Crustal structure across the Altyn Tagh Range at the northern margin of the Tibetan plateau and tectonic implications. *Earth and Planetary Science Letters*, *241*(3–4), 804–814. https://doi.org/10.1016/j.epsl.2005.11.003

Zhao, J., Zhang, P., Yuan, X., Gan, W., Sun, J., Deng, T., et al. (2019). Clockwise rotation of the Tarim basin driven by the Indian plate impact. *Науки о Земле и недропользование*, *42*(4), 425–436. https://doi.org/10.21285/2686-9993-2019-42-4-425-436

Zhao, L., Wen, L., Chen, L., & Zheng, T. (2008). A two-dimensional hybrid method for modeling seismic wave propagation in anisotropic media. *Journal of Geophysical Research*, *113*(B12), B12307. https://doi.org/10.1029/2008jb005733

Zhu, L. (2000). Crustal structure across the San Andreas Fault, southern California from teleseismic converted waves. *Earth and Planetary Science Letters*, *179*(1), 183–190. https://doi.org/10.1016/s0012-821x(00)00101-1

Zhu, L. (2009). Receiver function package (deconvolution and H-κ stacking) hk1.3 (Version 1.3) and Common-Conversion-Point (CCP) stacking codes ccp1.0 (Version 1.0) [Software]. Saint Louis University. Retrieved from https://www.eas.slu.edu/People/LZhu/home.html

Zhu, L., & Kanamori, H. (2000). Moho depth variation in southern California from teleseismic receiver functions. *Journal of Geophysical Research*, *105*(B2), 2969–2980. https://doi.org/10.1029/1999jb900322

References From the Supporting Information

Johnston, J. E., & Christensen, N. I. (1992). Shear wave reflectivity, anisotropies, Poisson's ratios, and densities of a southern Appalachian Paleozoic sedimentary sequence. *Tectonophysics*, *210*(1–2), 1–20. https://doi.org/10.1016/0040-1951(92)90124-o

Wang, X., Chen, L., Ai, Y., Xu, T., Jiang, M., Ling, Y., & Gao, Y. (2018). Crustal structure and deformation beneath eastern and northeastern Tibet revealed by P-wave receiver functions. *Earth and Planetary Science Letters*, *497*, 69–79. https://doi.org/10.1016/j.epsl.2018.06.007